

Received February 6, 2022, accepted February 20, 2022, date of publication February 24, 2022, date of current version March 8, 2022.

Digital Object Identifier 10.1109/ACCESS.2022.3154410

# Bearing Fault Detection in ASD-Powered Induction Machine Using MODWT and Image Edge Detection

VICTOR AVIÑA-CORRAL<sup>1</sup>, (Graduate Student Member, IEEE),  
JOSE DE JESUS RANGEL-MAGDALENO<sup>1</sup>, (Senior Member, IEEE),  
HAYDE PEREGRINA-BARRETO<sup>2</sup>, (Senior Member, IEEE),  
AND JUAN MANUEL RAMIREZ-CORTES<sup>1</sup>, (Senior Member, IEEE)

<sup>1</sup>Digital Systems Group, Electronics Department, Instituto Nacional de Astrofísica Óptica y Electrónica, Puebla 72810, Mexico

<sup>2</sup>Computer Department, Instituto Nacional de Astrofísica Óptica y Electrónica, Puebla 72810, Mexico

Corresponding author: Jose de Jesus Rangel-Magdaleno (jrangel@inaoe.mx)


**ABSTRACT** Today the industry depends on various types of three-phase induction machines, requiring operating at variable speeds to perform more complex processes. Therefore, it is vital to monitor their operation conditions to maintain the optimal efficiency of the processes they perform and avoid significant economic losses. The proposed work presents the design and development of a method for bearing damage detection based on Maximal Overlap Discrete Wavelet Transform and image processing for edge detection. Accuracies achieved with three types of damage exceed 90%. The signals for the test are acquired from seven different operating conditions for each type of damage. Supply comes from a power grid source and an adjustable speed drive. The Maximal Overlap Discrete Wavelet Transform is applied with different filtering levels to the three phases of the stator current, the magnitude of the filtered signals is acquired, a periodic two-dimensional array is generated and further smoothed by a Gaussian filter allowing the observation of patterns at the edges. Finally, the obtained images are scanned with a 2-D mask aiming to detect and count patterns associated to the fault detection process. Statistical analysis is performed over characteristic signatures obtained from the current magnitude of the three phases at different classes of damage and several mechanical load conditions.

**INDEX TERMS** Bearing fault detection (BFD), edge detection (ED), induction machine (IM), maximal overlap discrete wavelet transform.

## I. INTRODUCTION

An induction machine (IM) takes advantage of electromagnetism to convert electrical energy into mechanical energy in order to provide mechanical work [1]. Consequently, the invention of IM has generated increased demand in diverse industrial processes or applications such as drinking water supply, wastewater treatment plants, purification plants, water desalination plants [2], cooling, heating, building elevators, underground electric transport, electric trains, and electric cars, among others. These processes or applications require mostly asynchronous IM due to its robustness, standardization, and their ease of maintenance. However, the

unexpected interruption of some processes or applications has generated significant economic losses, so it has been considered vital to create models and monitor the current state of IM [3]. This motivates the scientific community to develop different detection methods. IM failures can occur because of internal or external causes. Among the internal causes are bearing damage, broken bars and loss of insulation in the windings, etc. [4], while external causes are due to sequence failures, phase loss or unbalance, undervoltage or overvoltage, harmonic distortion, among others [5]–[7]. Approximately 53% of IM failures are caused by bearing failures [4], [8]. The unexpected failures can lead to significant economic losses; therefore, it is essential to study the Bearing Failure (BF) that allows the development of new timely detection techniques.

The associate editor coordinating the review of this manuscript and approving it for publication was Feifei Bu .

In the relevant literature, several investigations have been made to address various methodologies and techniques for IM damage detection using digital signal processing; among them are recent works addressing rotor broken bar detection [9]–[11], damaged bearing detection [12]–[15], stator winding insulation fault detection [16]–[18], and multiple fault detection [19]–[22]. Many of these works have implemented several digital processing techniques, for example, the use of the Maximum Overlap Discrete Wavelet Transform (MODWT) [11], [23], and Motor Current Signature Analysis (MCSA) [10] for rotor broken bar detection, the use of the Stockwell transformer [13], [14], DWT [24], and statistical analysis [12] for damaged bearing detection, as well as the use of spectral resolution analysis for multiple fault detection [21], [25], and more. As a result, it can be concluded that the subject has already been meticulously researched, reporting accuracies ranging from 85 % to 100 % in damaged bearing detection [12], [26], [27]; however, many of these works are only adapted to specific failure conditions, but not to real faults, and the algorithms currently employed are specialized in finding failures under specific operating conditions, so it is necessary to subject any developed method to various operating and failure conditions in order to evaluate its accuracy correctly.

Other creative works that analyze the vibration signal, using techniques such as analysis for Squared Envelope Based Spectral Kurtosis (SESK) [28]. Up to now, the vibration-based bearing fault diagnostic is widely used [13], [24], [29]–[32], recent research has been found that takes advantage of the benefits of the MODWT for the detection of damage in gearboxes or bearings mainly by vibration signals, because the MODWT is suitable for the decomposition of the complete cycle signal of bearings and gears. The authors who use the MODWT or some of its variants as the MODWPT emphasize that one of the main advantages is that it does not use subsampling, which gives a higher resolution of the signal [33]–[35]. Nevertheless, very few MODWT-based works have been found for current signals when the motor is powered by adjustable speed drive (ASD) or other electronic drive equipment [23].

This work presents a method to detect localized and distributed damage in the front bearing of a three-phase asynchronous induction machine by using MODWT in combination with some linear transformations, filtered texture image processing, and statistical classifiers for stator current analysis. As a result, the type of localized and distributed damage in the front bearing of the induction machine is detected and discerned in power grid source (PGS) or ASD applications. The methodology is based on analyzing the torque variation using the current magnitude of the three phases. The obtained results show accuracies greater than 90% for all cases.

## II. THEORETICAL BACKGROUND

Localized bearing damage is generally associated with a frequency band that is observed as a vibration frequency or in the frequency components that modulate the stator current.

Various models have been presented to represent this based on their structure. The mechanical frequency  $f_m$  caused by the passage of the ball, which produces a vibration generated by the damage at a single point located in the various zones of the bearing, can be determined by (1), while the current frequency in the sidebands corresponding to the damage is obtained from (2) [36].

$$\left. \begin{aligned} f_o &= \frac{N_b}{2} f_r \left( 1 - \frac{R_b}{R_c} \cos \beta \right) \\ f_i &= \frac{N_b}{2} f_r \left( 1 + \frac{R_b}{R_c} \cos \beta \right) \\ f_b &= \frac{R_c}{2R_b} f_r \left( 1 - \left[ \frac{R_b}{R_c} \cos \beta \right]^2 \right) \\ f_c &= \frac{1}{2} f_r \left( 1 - \frac{R_b}{R_c} \cos \beta \right) \end{aligned} \right\} f_m \quad (1)$$

$$f_{bf} = |f_s \pm k f_m| \quad (2)$$

where  $N_b$  is the number of balls in the bearing,  $R_b$  is the radius of the ball,  $f_r$  is the rotation frequency,  $R_c$  is the pitch radius,  $\beta$  is the contact angle between the ball and the ball bearing races (see Fig. 1),  $f_i, f_b, f_o$ , and  $f_c$  are the mechanical frequencies due to the inner raceway fault, the ball fault, the outer raceway fault, and the cage effect respectively,  $k$  is a natural number,  $f_s$  is the electrical frequency at which the motor is powered,  $f_{bf}$  is the frequency observed as the sidebands of the BF in the current signal. The absolute value is used in (2) because negative frequencies are not considered.

### A. MAXIMAL OVERLAP DISCRETE WAVELET TRANSFORM (MODWT)

This transformation enables multi-resolution analysis (MRA) similar to DWT. One of the main advantages of MODWT over DWT are: the use of vectors of the same length as the original signal  $x(n)$  to represent decomposition levels [11], thanks to its lack of downsampling, more information is retained and the acquired signals are smoothed out for higher levels of transformation, and the use of MODWT to create an MRA makes the choice of wavelet filter less critical, so easier to process filters such as Haar with only two points can be chosen. However, its main disadvantage is the amount of memory resources it requires compared to DWT.

Figure 2 shows the construction process of a MODWT as well as the corresponding filters. Take special attention to the fact that due to upsampling, for a Daubechies wavelet it is

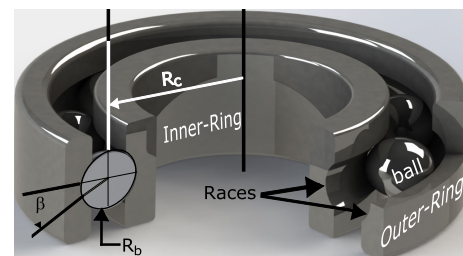
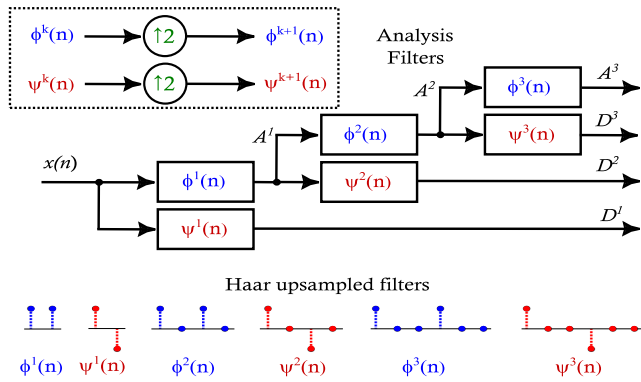


FIGURE 1. Structure of bearing 6205, its properties and main parts.



**FIGURE 2.** Basic structure of MODWT, in the upper part is shown the expansion process of the scale and wavelet function by means of upsampling, in the lower part is shown the value of the filter coefficients where the maximum amplitude is  $1/\sqrt{2}$  for all cases.

not necessary to decrease the amplitude of the filter ratios as would be done in a conventional wavelet transform. It is no longer necessary to worry about filling in the missing spaces in the discretization to dilate the function. Therefore, the MODWT is a particular type of wavelet transform that is easy to implement.

### III. METHODOLOGY

#### A. DATA ACQUISITION

Figure 3 shows the block diagram used for bearing damage detection by MODWT. A DAS acquisition stage is also required, which is carried out employing hardware and consists of an analog conditioning stage, a digital conversion, and acquisition stage, which is responsible for sending the signals to a Personal Computer (PC). As can be seen in the block diagram, the current signals are studied in two modes, the current acquired from the stator and the current squared from the stator can be studied; only in the latter case must the signal be considered as doubling its frequency.

The fixed sampling length and full-cycle acquisition procedure allow a fixed data acquisition analysis. This procedure aims to set a fixed acquisition of 614.4 cycles per sample as shown in (3). This is obtained with a fixed 65535 data length ( $Data_{len}$ ), and a normalized data rate acquisition ( $Data_{rate}$ ) (6400 data/s). As a result, the adjustable sampling rate ( $f_{samp}$ ), for any IM operational frequency ( $f_s$ ), is calculated in (4). The  $f_{samp}$  is used in the data acquisition system as sampling rate configuration.

$$Cycle_{samp} = \frac{Data_{len}}{Data_{rate}} 60Hz = 614.4(cyc/sample) \quad (3)$$

$$f_{samp} = \frac{Data_{rate}}{60Hz} f_s \quad (4)$$

#### B. SIGNAL TREATMENT

When analyzing the MCSA, five sets three-phase signals will be generated whose magnitude is determined by (5). This magnitude is used to form a bidimensional array in which some bands that repeat periodically can be seen.

The array must be built so that the total number of pixels of width corresponds to the exact cycles of the signal. Later a little noise and spurious components are eliminated using a Gaussian filter in 2D. The filtered signal is binarized, where if desired, a small hysteresis to eliminate unwanted noise can be included. Once the signal is binarized, it is possible to obtain fine edges of one-pixel width using the Laplacian. These edges are analyzed by a set of masks that determine the number of matching patterns in the two-dimensional array, which allows obtaining a characteristic distribution function for each type of case utilizing the calibration with known signals.

The signals are classified by a detection stage that identifies the test signals according to their similarity to the calibrated probability distribution, whose typical behavior is a log-normal, using hypothesis tests with  $\alpha = 0.1\%$ , giving an idea of the low overlap between the categories to be tested. This is done for both the original signal and the four MODWT decomposition levels. The results of all decomposition levels and the original signal must be classified in the same category to which they are assigned. Priority is given to healthy classification, so if it falls into an overlap region between healthy and damaged, it will be classified as healthy as a priority, provided that all levels have also been classified in the same way, so it is possible for a damaged bearing to be classified as healthy if all levels were classified as such, but not vice versa.

$$i_r = \|\vec{i}_{abc}\| = \sqrt{\frac{2(i_a^2 + i_b^2 + i_c^2)}{3}} \quad (5)$$

To obtain good results with the proposed methodology, it is necessary to eliminate the DC-Offset components and normalize the phase currents in amplitude. This is possible if the signals are subtracted from their mean and divided by their standard deviation.

If the three current phases are squared or multiplied by themselves, a three-phase set of signals is produced that oscillates at 120 Hz, whose phase balance is considered ideal. The above steps can be performed for both the current and square current of the motor. It should be noted are that when the current is squared, it tends to change its amplitude and also adds a DC-offset value which is recommended to be eliminated in order to appreciate better the variations in the magnitude of the  $\vec{i}_{abc}^2$  motor's square current vector. The block diagram in Fig. 3 shows that both MCSA and MSCSA can be used.

#### C. SELECTION OF LEVELS 4 TO 7 OF THE MODWT

The wavelet levels of the signal are extracted by the matlab function modwt, which generates a multi-resolution array containing the detail coefficients  $D^1, D^2, D^3, \dots, D^{15}$ , of whose in this case only  $D^4, D^5, D^6$ , and  $D^7$  are of interest. Figures 4 and 5 show the information content of the levels of interest, where the signal elongation between levels 4 and 7 is greatest. The Haar-type Wavelet transform has been used. In addition, in the first levels of the transformation, this

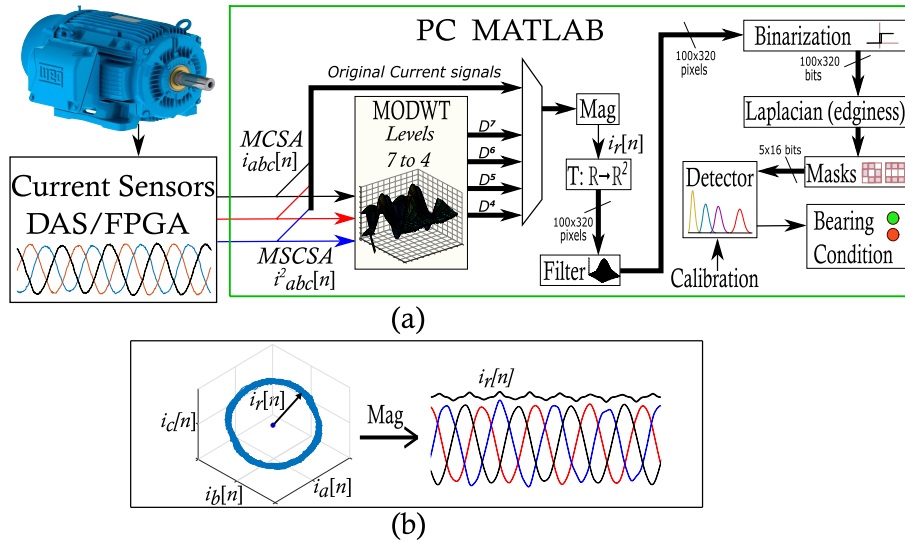


**FIGURE 3.** (a) Block diagram explaining the methodology used. (a)(b) Principle to obtain the magnitude of the current vector.

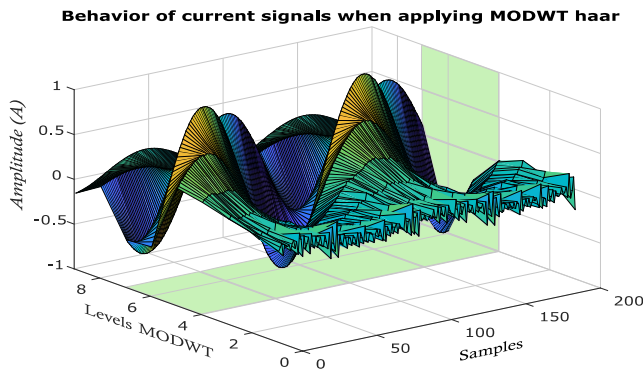


**FIGURE 4.** MRA using MODWT levels  $D^1$  to  $D^9$ , it is observed that the phase current information is retained in the shaded region corresponding to levels 4 to 7.

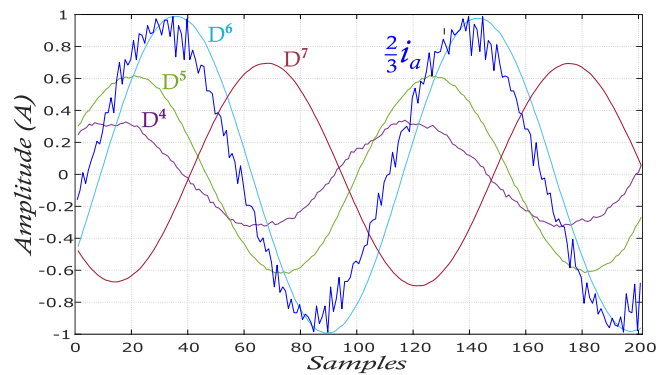


**FIGURE 5.** Waveforms of the detail coefficients  $D^4$  to  $D^7$  of the MODWT, and original signal obtained from a motor fed by an ASD tuned to 60 Hz, the amplitude of the original current signal has been attenuated at a rate of  $2/3$ .

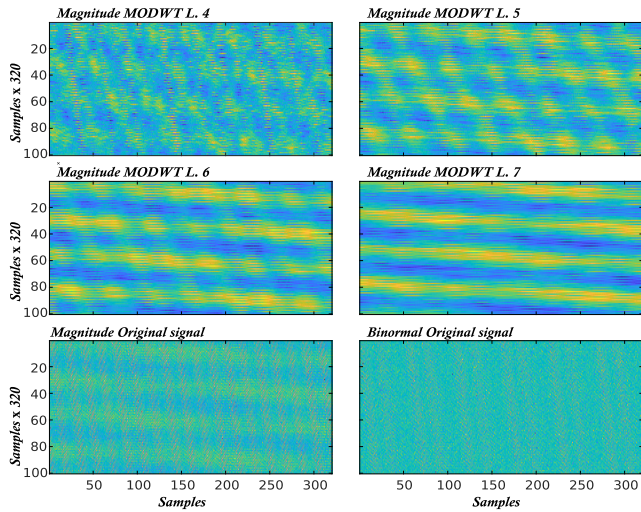
type of filter eliminates much of the high-frequency noise introduced by the switching of the frequency converter.

#### D. IMAGE PROCESSING

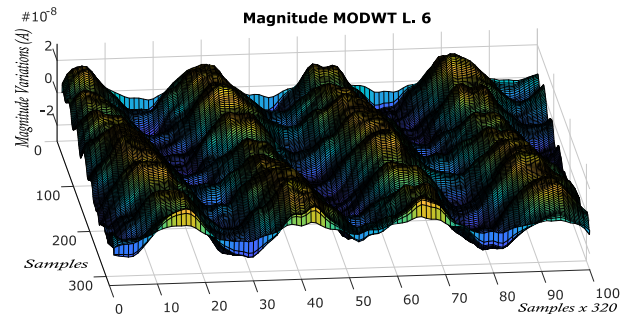
The signal acquired by the motor current magnitude has a periodic behavior, so if exact cycles are repeated in each line of a two-dimensional array, a stripe pattern will be observed (see Fig. 6). Since the signal is sampled at 6,400 samples per second, one cycle of the signal at 60 Hz cannot be represented with a whole number of samples, but three cycles require 320 exact samples, which defines the number of pixels wide used in the two-dimensional array. Therefore, the height is defined as 100 pixels so that the 2D array is made up of a total of 32,000 pixels; this is equivalent to 5 seconds of signal for a 60 Hz operating frequency. For other operating frequencies, the sampling frequency is set so that an array of 320 pixels wide is always maintained, that is, if a motor is working at 30 Hz, its current will be sampled at 3,200 samples per second.

Figure 6 shows six two-dimensional arrays, the first 4 in the upper part correspond to the 2D array for each level of MODWT decomposition ( $D^4, D^5, D^6$ , and  $D^7$ ). The last two in the lower part corresponding to the original signal, where one is the magnitude of the vector measured from the center of the path formed by the current vector and measures the normal variations to the circular path (radial variations  $i_r$ ). While the figure on the right at the bottom shows the binormal variations (axial variations  $i_\gamma$ ), it is usually made up of only undesirable noise.

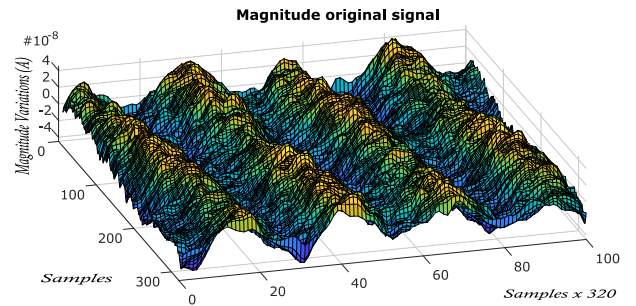
Figure 7 shows the relief of magnitude variations for level 6 of the transformation and the original signal. It can be noticed that when the signal is concatenated with itself, a periodic pattern is formed, in which it is possible to appreciate that there is too much noise, producing a very rough surface. In Fig. 6, it is clear that the behavior is less rough as the transformation level increases, so each transformation level contributes different patterns; however, the binormal components (axial) only contribute unwanted noise.



**FIGURE 6.** Two-dimensional arrangements corresponding to the detail coefficients for the transformation levels 4, 5, 6, 7 and current magnitude of the original signal and its binormal variation, as indicated in the header of each image.



(a)



(b)

**FIGURE 8.** Reliefs of the two-dimensional arrays once filtered. (a) Magnitude variation of  $D^6$ . (b) Magnitude variation of the original signal.

where  $\sigma_p$  and  $\sigma_k$  are the standard deviations in the two directions that define the bell's opening in the horizontal and vertical directions respectively,  $p_o$  and  $k_o$  indicate the location of the pixel that corresponds to the bell's maximum. In this case the values were chosen:  $p_o = 50$ ,  $k_o = 160$ ,  $\sigma_p = 200$  and  $\sigma_k = 1800$ .

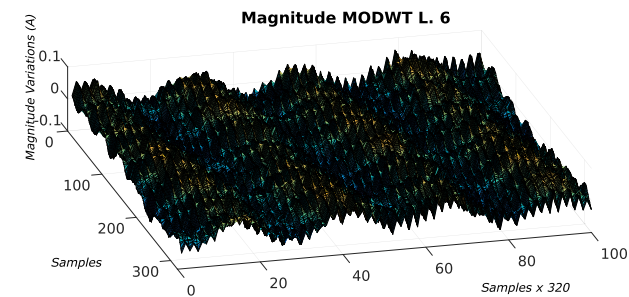
Figure 8 shows the two dimensional arrays (of fig. 7) filtered, it can be seen the smoother surfaces where periodic patterns are easily distinguishable.

#### F. BINARIZATION WITH THRESHOLD AND HYSTERESIS

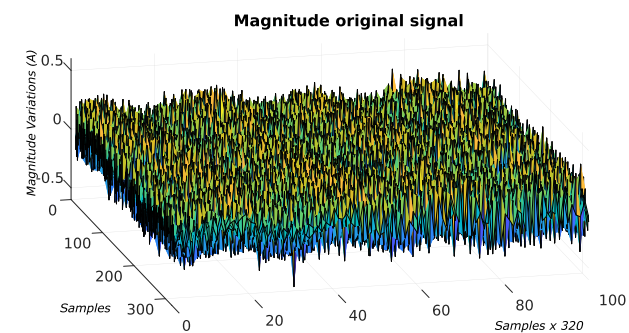
As shown in Fig. 7 and Fig. 8 the DC component has been removed, allowing the threshold to be zero. Since the plots have a reasonably smooth behavior, the hysteresis value for the threshold can be minimal or zero compared to the oscillation amplitude of the observed surfaces. Perhaps the hysteresis could be more useful in the case of Fig. 8.b, which corresponds to the magnitude variation of the original signal.

The threshold allows everything above the set threshold value to become one, while everything below is zero. The hysteresis level reduces the generation of islands or points near the transition region that could be considered as unwanted noise. Fig. 9 shows the 2D pattern before binarization and Fig. 10 shows the binarized pattern in image format.

Once the image has been binarized using Laplacian, it is possible to obtain a fine edge one pixel wide. By analyzing these fine edges, it is possible to determine the condition of the bearing. Figure 11 shows the behavior of the edges obtained from the 2D arrays.



(a)



(b)

**FIGURE 7.** Reliefs of the two-dimensional arrays generated from the current vector, the level of DC offset has been eliminated. (a) Magnitude variation of  $D^6$ . (b) Magnitude variation of the original signal.

#### E. GAUSSIAN FILTER

The 2D arrays were filtered by a Gaussian function to reduce noise. The Gaussian filter is defined by the following equation:

$$G(p, k) = \frac{1}{2\pi\sigma_p\sigma_k} e^{-\frac{1}{2}\left(\frac{(p-p_o)^2}{\sigma_p^2} + \frac{(k-k_o)^2}{\sigma_k^2}\right)} \quad (6)$$

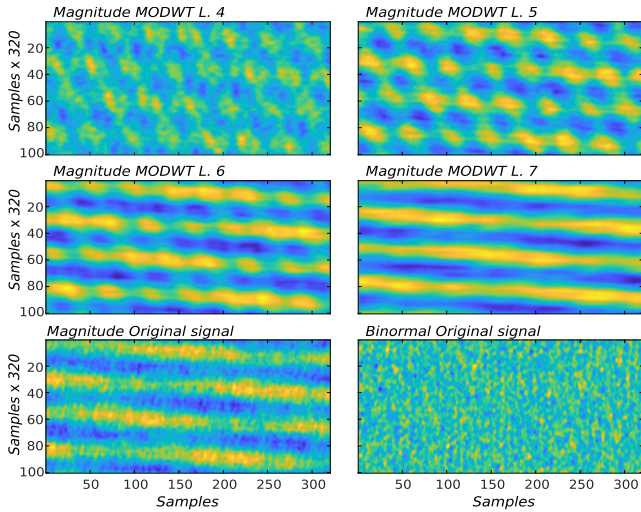


**FIGURE 9.** Filtered unbiased two-dimensional arrays corresponding to the detail coefficients for the transformation levels 4, 5, 6, 7 and current magnitude of the original signal and its binormal variation, as indicated in the header of each image.

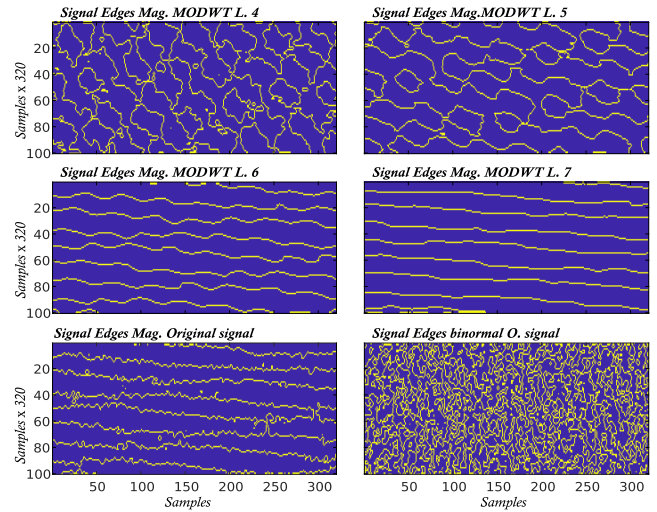


**FIGURE 11.** Detection of edges in arrays corresponding to the detail coefficients for the transformation levels 4, 5, 6, 7 and current magnitude of the original signal and its binormal variation, as indicated in the header of each image.

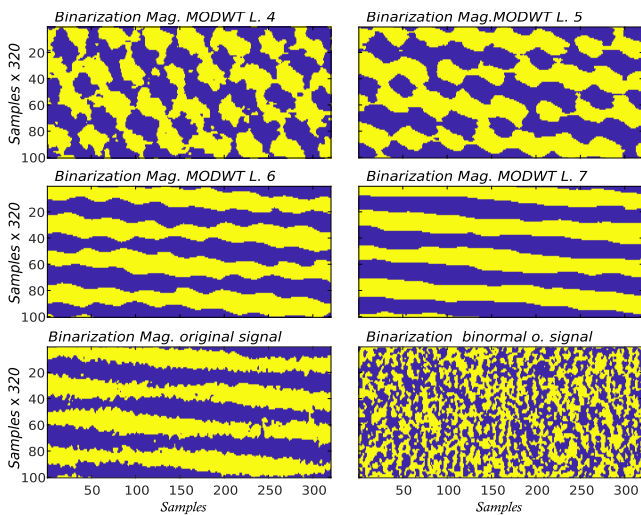


**FIGURE 10.** Two-dimensional arrangements in values 0 and 1 corresponding to the detail coefficients for the transformation levels 4, 5, 6, 7 and current magnitude of the original signal and its binormal variation, as indicated in the header of each image.

**G. IDENTIFYING PATTERNS WITH MASKS**

The edge behavior analysis is performed by scanning a 9-pixel combinatorial square mask containing a central horizontal strip of pixels of value 1 (see Fig. 12), while the other pixels are zero, by scanning the two-dimensional matrix for patterns identical to it, leaving a 2-pixel margin at the boundaries (as there may be unwanted distortion at the matrix margin). As the mask scans the array, the number of patterns matching the mask is counted as a cumulative sum. Figure 12 shows the basic principle of using the mask. The sweep is first done horizontally; each time it stops, it compares the bits in the region against the mask being tested. If all the bits

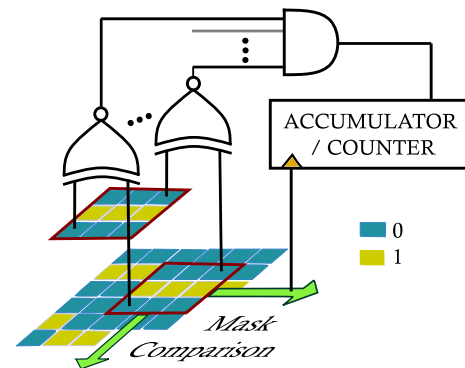


**FIGURE 12.** Basic principle for sweeping and comparison of the mask with the two-dimensional arrangement containing edges.

are the same, the counter increases; otherwise, it continues to traverse the array.

Other 9-pixel masks were also studied in which the pattern is not horizontal, and even 15-pixel rectangular masks were tested, but the mask with the most relevant results are obtained is the one with the horizontal edge; however, it is left to future research to test different combinations of masks simultaneously.

In the graphs of Fig. 11 it is observed that each of the figures contains different number of horizontal patterns, these horizontal patterns are counted for each bearing condition behaving as a fingerprint for each case, the detector uses the number count of horizontal patterns observed and thus by means of the log-normal probability distributions classifies the type of damage.

The number of patterns matching the mask corresponds typically to some damage condition so that if the experiment is repeated, a log-normal probability distribution is produced. This was determined by observing the shape of the acquired

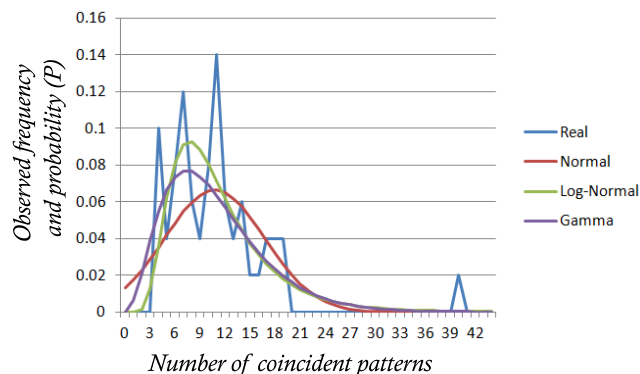


**FIGURE 13.** Fitting the data to four possible probability distributions, in this case, the distribution that best fit is the log-normal, given the skewness of the data distribution.

data asymmetric distribution, and the accuracy was tested using normal and log-normal distributions, with the accuracy in all cases being exceeded by the log-normal distribution (see Table 2).

Figure 13 shows the counting behavior of one of the masks tested for a specific batch of 50 healthy case signals. In this case, to illustratively highlight the log-normal behavior, a mask with a diagonal band of negative slope was used, and a wavelet filtered signal was also used, which presents mostly horizontal patterns, so the pattern count was not higher than 42 patterns. Hypothesis tests were performed to 3 types of distributions: Normal, Log-Normal and Gamma, which determined that the best fit was the Log-Normal distribution. In addition to the same tests performed in Table 1, there were also performed with Normal distribution, noting a slight decrease in the accuracy achieved. As we can observe, the normal distribution does not present an adequate accuracy value for fault type classification, however it is worth noting that the accuracy achieved for only damage condition detection exceeded the accuracy of the log-normal distribution.

As we can observe, the normal distribution does not present an adequate accuracy value for fault type classification, however it is worth noting that the accuracy achieved for only damage condition detection slightly exceeded the accuracy of the log-normal distribution only by a few tenths (see Table 1). As a result, it was decided to choose the log-normal distribution instead of the normal one, leaving as future work the study with the normal distribution.

In Figure 13 the vertical axis corresponds to the probability, while the horizontal axis is the count of matching patterns in each test. The characteristic probability distribution is established for a relatively high acceptance region since the value of  $\alpha = 0.1\%$ . On the other hand, the use of a log-normal probability distribution allows a better fit to the rejection regions (distribution tails) in an asymmetric way, which increases the accuracy and avoids unnecessary overlaps. Finally, once the sum of the patterns found has been accumulated, it must be compared with the limits established for the case of healthy bearing and damaged bearing, thus classifying the set of

signals tested. In order to assign a healthy category to a bearing, all the accumulators, for each level of wavelet and the original signal, must be classified simultaneously in that category, which makes the test more rigorous. Furthermore, using the MODWT allows a search for faults under different resolutions.

#### IV. EXPERIMENTAL SETUP

##### A. TEST BENCH SETTINGS

For this work, the experimental tests are carried out through a three-phase IM WEG 00118ET3EM143TW, 1HP, 1800RPM, 220VAC@60Hz, and 2.98A. The IM nominal current is used as the maximum value of the load applied. The load is mechanically generated; this sets the loaded condition when the rotor is attached with the belt, consuming 60% of the IM nominal current. One healthy bearing and three different damaged bearings are used for bearing 6204 (see FIGURE14). The first damage presented is the outer raceway with a hole of 1.58 mm diameter (HOLE) (FIGURE14.a). Next, the bearing BALL damage (BALL) is obtained by a drilling tool with a diameter of 1.58mm (FIGURE14.b). Finally, Distributed Damage Case (DDC) is presented employing a corroded bearing (FIGURE14.c). Each damaged bearing is placed on the front cover of an IM set. The power source is configured under seven conditions. The first one is the power grid source (PGS); the rest are obtained from an adjustable speed drive (ASD) configured at 2.5kHz switching frequency, the lowest frequency available, which allows a high ripple order; the operational frequency is set to 60Hz, 50Hz, 40Hz, 30Hz, 20Hz, and 10Hz. The three-phase current data are measured by a digital acquisition system (DAS) and FPGA set. The DAS subsystem is comprised of: three ACS758LCB-050B current sensors, a hardware signal conditioning stage is implemented using the OP177, and the ADS7841P is used as an analog to digital converter stage for the three-phase currents. The digital data are sent to an FPGA Xilinx family on a Digilent Genesis-2 board through serial port interface (SPI) protocol. The FPGA stores the acquired data using the ( $f_{samp}$ ) configuration shown in (4). In order to enable/disable the PGS or the ASD, the FPGA also sends the RUN/STOP command to an

**TABLE 1.** Optimization of the  $\alpha$  value using normal distribution.

$\alpha$	GEN	S.P.	DSTR	FAULT
0.5%	82.32%	82.19%	84%	95.75%
0.4%	83.93%	84.14%	85.36%	96.25%
0.3%	87.89%	88.95%	87.21%	95.64%
0.2%	87.25%	88.19%	88.86%	96.82%
0.15%	90.39%	92.71%	87.86%	95.21%
0.1%	88.39%	90.19%	88.36%	95.43%
0.05%	89%	91.95%	87.5%	94.57%

$\alpha$  optimal 0.15% for classification  
 $\alpha$  optimal 0.2% for fault detection

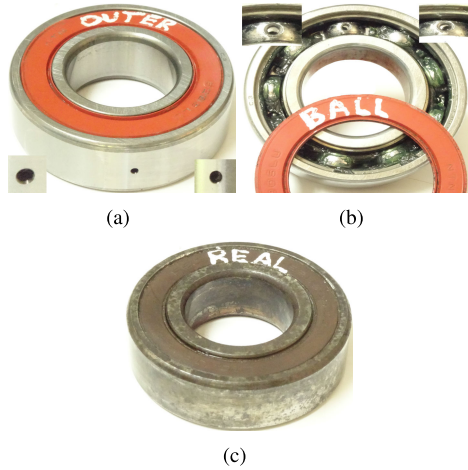


**FIGURE 14.** Bearing damages studied. (a) Outer-race damage (1.58mm hole). (b) Bearing BALL damage (1.58mm hole). (c) Corrosion damage (distributed damage).

**TABLE 2.** Optimization of the  $\alpha$  value using log-normal distribution.

$\alpha$	GEN	S.P.	DSTR	FAULT
0.5%	84.96%	85.86%	84.64%	95.68%
0.4%	86.11%	87.19%	85.21%	95.29%
0.3%	85.39%	85.9%	86.93%	96.36%
0.2%	90.14%	92%	88%	95.32%
0.15%	90.39%	92.71%	87.86%	95.21%
0.1%	91.18%	94.38%	88%	95.07%
0.05%	91.04%	94.62%	87.5%	93.75%

$\alpha$  optimal 0.1% for classification  
 $\alpha$  optimal 0.3% for fault detection

electromagnetic switch. This is done by a relay board that allows the selection of the IM power source.

**B. ALGORITHMS USED**

Two algorithms (MCSA and MSCSA), based on the methodology proposed in section III, have been programmed in MATLAB. For MCSA, the damage detection results obtained from the distributed damage analysis are presented in Table 1 (where the GEN label refers to the overall accuracy to distinguish between different types of damage, while S.P. refers to the ability to distinguish single point damage versus healthy, DSTR refers to the ability to distinguish distributed damage from healthy and FAULT refers only to distinguishing any damaged case from healthy case). To determine the accuracy of the presented algorithms, the bearing damage was compared with the healthy bearing under the same operating and loading conditions. The experiment is repeated ten times at random.

**C. COMPARISON WITH OTHERS METHODS**

In Table 4 several methodologies studied in the last 5 years are presented and compared with this work. Many of the methodologies presented reach higher accuracies than the present work, however some of them are based on

**TABLE 3.** Accuracy with and without load for  $\alpha = 0.1$ .

Load condition	GEN	S.P.	DSTR	FAULT
Unload	93.86%	96.29%	91.86%	97.29%
Load	88.5%	92.48%	84.14%	92.6%
Total	91.18%	94.38%	88%	95.07%

artificial intelligence which implies a much higher computational cost than this technique. Nevertheless, there are also quite simple methodologies presented here with quite promising, such as [41]. All in all, however the proposed methodology is interesting and novel and can be applied in other fields of study. In the appendix A, a study of the computational cost of this technique in comparison with others is made, see Table 11.

**V. DISCUSSION**

In order to analyze the accuracy of the test and to study its ability to distinguish between the different classes of damage at mechanical load conditions, confusion matrices were performed. The best results to distinguish between classes are obtained using the log-normal distribution reaching an overall accuracy of 91.18% for a value of  $\alpha = 0.1$ . However, it should be kept in mind that if it is a matter of distinguish the damaged case from the healthy case, the appropriate value of  $\alpha$  is 0.3 reaching an overall accuracy of 96.36% (this accuracy is based on classifying the damage for 50 healthy and 150 damaged cases of three types according to the generated confusion matrices), see Table 2. The method was tested to distinguish between various bearing conditions to evaluate the test.

Table 3 shows the performance of the test with and without load, the results without load are quite promising. However it is observed that when the IM is subjected to load it costs the method to achieve a good accuracy for the DDC (84.14%), also the methodology presents problems to distinguish various classes of damage (GEN 88.5%), but the accuracy is high for detecting damage at a single point (HOLE 92.48%). In addition to these disadvantages with a  $\alpha = 0.1$  a high accuracy is achieved to discern between a healthy and a damaged case (FAULT 92.6%), this is good since what is sought is to detect the damage condition and not what type of damage the bearing has.

Tables 5 and 6 also use  $\alpha = 0.1$ , in them the accuracy of the method to classify between the different types of damage is obtained, however with the data presented the other accuracies presented in Table 3 can be obtained, the accuracies in Table 5 are good most of the different feed conditions either PGS or ASD. For the loaded case (Table 6) there is a decrease in accuracy for the 60 Hz PGS because the DDC is classified as a healthy bearing 30% of the attempts, likewise for the 30 Hz ASD the DDC is classified as healthy 18% of the attempts, for the 20 Hz ASD 44% of the attempts and



**TABLE 4. Comparison between the proposed technique and other existing methods in the literature. (ORW: Outer Raceway; IRW: Inner Raceway; RE: Rolling Element; PGS: Power Grid Source; ASD: Adjustable Speed drive).**

Year	Methodology	Load (%)	Fault type	Severity (mm)	Source	Accuracy (%)
2018 [37]	Kolmogorov-Smirnov Test is applied to current signal to detect fault bearing.	0 and 100	ORW	3.1	PGS	96.67
2018 [38]	Empirical Wavelet Transform is applied to vibrations signal, then the Fuzzy Entropy is applied for feature extraction, and Support Vector Machine is used for classification.	0, 50, 100, and 150.	ORW, IRW, and RE	0.18, 0.36, 0.53, and 0.71.	PGS	96.67
2019 [31]	The spectral image of vibration is used to detect the bearing fault with Convolutional Neural Networks.	–	ORW, IRW, and RE	–	ASD	98.26
2019 [39]	Co-occurrence matrix of Time Frequency Imaging blocks of vibrations are used for feature extraction and the Linear Support Higher Order Tensor Machine is used for classification.	0, 50, 100, and 150.	ORW, IRW, and RE	0.18, 0.36, 0.53, and 0.71.	PGS	96.38
2019 [40]	Mel-frequency cepstral coefficients and delta cepstrum technique are used in vibrations to feature extraction, and a Convolutional Neural Network Spectral Kurtosis-based is used for classification.	0, 50, 100, and 150.	ORW, IRW, and RE	0.18, 0.36, 0.53, and 0.71.	PGS	98.76
2020 [41]	The amplitudes of the current signals are monitored directly using the half cycle of the waveform and employ Artificial Neural Network for classification.	0 and 100	Distributed	–	ASD	> 71
2020 [32]	The Discrete Wavelet Package Transform and the Fourier Transform are used to feature generation, and Adaptive Neural-Fuzzy Inference System are employed for classification.	0, 50, 100, and 150.	ORW, IRW, and RE	0.18, 0.36, 0.53, and 0.71.	PGS	99.83
2020 [42]	The Continuous Wavelet Transform is used for feature extraction, and a Convolutional Neural Network and Support Vector Machine are used for classification.	0, 50, 100, and 150.	ORW, IRW, and RE	0.18, 0.36, 0.53, and 0.71.	PGS	98.89
2021 [42]	Statistical tests are applied to stator current signals for bearing fault detection (ASD-powered).	0 and 100	ORW, RE, and distributed.	1.58	ASD and PGS	97.10
2021 [30]	Vibration analysis and shallow Neural Networks.	Variable: 0 to 100	ORW, IRW, and RE.	-	ASD	> 95
2021 [23]	Mechanical and electrical faults MODWT and Lightweight 1D CNN (ASD-powered).	0 and 100	ORW	1.60	ASD and PGS	99.84
This paper	MODWT and Image Edge Detection (ASD-powered).	0 and 100	ORW, RE, and distributed.	1.58	ASD and PGS	94.68 - 97.74

**TABLE 5. Confusion matrix for unloaded tests using log-normal distribution ( $\alpha = 0.1$ ).**

Operation	Condition	HEALTH	HOLE	BALL	DDC	UNDEF	Accuracy
60 Hz PGS	HEALTH	48	0	0	0	2	90%
	HOLE	0	50	0	0	0	
	BALL	0	0	48	0	2	
	DDC	15	0	0	34	1	
60 Hz ASD	HEALTH	49	0	0	0	1	90.5%
	HOLE	6	43	0	0	1	
	BALL	0	0	44	0	6	
	DDC	0	0	0	45	5	
50 Hz ASD	HEALTH	49	0	0	0	1	92%
	HOLE	5	43	0	1	1	
	BALL	0	0	47	0	3	
	DDC	0	1	0	45	4	
40 Hz ASD	HEALTH	48	0	0	0	2	96%
	HOLE	0	50	0	0	0	
	BALL	0	0	49	0	1	
	DDC	0	0	0	45	5	
30 Hz ASD	HEALTH	48	0	0	0	2	96.5%
	HOLE	0	50	0	0	0	
	BALL	0	0	50	0	0	
	DDC	0	0	0	45	5	
20 Hz ASD	HEALTH	49	0	0	0	1	96%
	HOLE	0	50	0	0	0	
	BALL	0	0	49	0	1	
	DDC	0	0	0	44	6	
10 Hz ASD	HEALTH	49	0	0	0	1	96%
	HOLE	0	50	0	0	0	
	BALL	0	0	48	0	2	
	DDC	2	0	0	45	3	

Accuracy = 93.86% Standard Deviation=2.90%,  $\alpha = 0.1\%$ .

**TABLE 6. Confusion matrix for loaded tests using log-normal distribution ( $\alpha = 0.1$ ).**

Operation	Condition	HEALTH	HOLE	BALL	DDC	UNDEF	Accuracy
60 Hz PGS	HEALTH	47	0	0	0	3	87%
	HOLE	0	46	0	0	4	
	BALL	0	0	47	0	3	
	DDC	15	0	0	34	1	
60 Hz ASD	HEALTH	44	0	0	0	6	93%
	HOLE	0	49	0	0	1	
	BALL	0	0	46	0	4	
	DDC	0	0	0	47	3	
50 Hz ASD	HEALTH	47	0	0	0	3	93.5%
	HOLE	0	49	0	0	1	
	BALL	0	0	44	0	6	
	DDC	0	0	0	47	3	
40 Hz ASD	HEALTH	45	0	0	0	5	93.5%
	HOLE	0	47	0	1	2	
	BALL	0	0	46	0	4	
	DDC	0	0	0	49	1	
30 Hz ASD	HEALTH	46	0	0	0	4	89.5%
	HOLE	0	47	0	0	3	
	BALL	0	0	46	0	4	
	DDC	9	0	0	40	1	
20 Hz ASD	HEALTH	46	1	0	0	3	82%
	HOLE	0	46	0	1	3	
	BALL	0	0	45	0	5	
	DDC	22	0	0	27	1	
10 Hz ASD	HEALTH	46	0	0	0	4	81%
	HOLE	0	47	0	0	3	
	BALL	0	0	45	0	5	
	DDC	25	0	0	24	1	

Accuracy = 88.50% Standard Deviation=5.35%,  $\alpha = 0.1\%$ .

for the 10 Hz ASD 50% of the attempts. However, for 60, 50 and 40 Hz ASD the DDC is not classified as healthy any of the occasions, these data show that it is more complex but

not impossible to detect DDC than point damage caused in the laboratory.

TABLE 7. Summary of all unloaded test for MCSA.

Operation	HOLE	BALL	DDC
60 Hz PGS	99.9% ± 0.01%	99.9% ± 0.01%	99.5% ± 0.53%
60 Hz ASD	99.9% ± 0.01%	99.9% ± 0.01%	99.5% ± 0.53%
50 Hz ASD	76.6% ± 9.83%	85.6% ± 6.31%	81.8% ± 7.73%
40 Hz ASD	98.8% ± 3.12%	97.9% ± 3.78%	97.4% ± 3.24%
30 Hz ASD	99.5% ± 0.53%	99.9% ± 0.32%	99.9% ± 0.01%
20 Hz ASD	99.9% ± 0.01%	99.9% ± 0.01%	99.9% ± 0.01%
10 Hz ASD	99.9% ± 0.01%	99.9% ± 0.01%	99.9% ± 0.01%

Global Accuracy = 96.92, % Standard Deviation=1.71%

TABLE 8. Summary of all loaded test for MCSA.

Operation	HOLE	BALL	DDC
60 Hz PGS	98.8% ± 1.23%	99.4% ± 0.7%	99.3% ± 0.67%
60 Hz ASD	97.2% ± 5.07%	96.6% ± 8.66%	98.3% ± 2.63%
50 Hz ASD	65% ± 7.97%	71.9% ± 14.36%	76.8% ± 24.13%
40 Hz ASD	97.7% ± 4.64%	99.7% ± 0.48%	94% ± 11.63%
30 Hz ASD	89.5% ± 17.93%	85.7% ± 16.55%	89.7% ± 13.98%
20 Hz ASD	99.7% ± 0.48%	99.7% ± 0.48%	99% ± 1.05%
10 Hz ASD	96.4% ± 3.75%	87.8% ± 6.73%	98.9% ± 1.6%

Global Accuracy = 92.43, % Standard Deviation=6.89%

TABLE 9. Summary of all unloaded test for MSCSA.

Operation	HOLE	BALL	DDC
60 Hz PGS	88.1% ± 2.85%	91.3% ± 2.91%	92.7% ± 3.37%
60 Hz ASD	88.7% ± 5.76%	92.1% ± 5.24%	93.5% ± 3.41%
50 Hz ASD	66.5% ± 14.21%	66.5% ± 13.88%	67.1% ± 12.2%
40 Hz ASD	90.01% ± 10.89%	88.9% ± 9.84%	91.4% ± 11.35%
30 Hz ASD	99.3% ± 0.48%	99.9% ± 0.01%	99.9% ± 0.01%
20 Hz ASD	99.9% ± 0.01%	99.5% ± 0.53%	99.9% ± 0.01%
10 Hz ASD	99.9% ± 0.01%	99.9% ± 0.01%	99.9% ± 0.01%

Global Accuracy = 91.22, % Standard Deviation=4.61%

In order to subject the method to a more rigorous analysis, a value of  $\alpha = 0.3$  was used to classify healthy and damaged bearing signals, using a set of 100 signals of which, 50 were with damage and 50 without damage, also different power supply sources were used, obtaining the results in Tables 7 and 8. Tests again reveal that accuracy decreases when load is applied to MI.

When performing experiments with MSCSA the opposite becomes evident, the accuracy without load decreases and the accuracy with load increases, see Tables 9 and 10, it is important to note that the signal frequency doubles as the signal is squared and regions of the signal that were previously ignored with MCSA are analyzed.

On the other hand, note in Tables 7 to 10 that the accuracy at 50 Hz decreases because there were amplitude oscillation problems with the ASD output at that specific frequency, affecting the quality of the database at that specific frequency.

TABLE 10. Summary of all loaded test for MSCSA.

Operation	HOLE	BALL	DDC
60 Hz PGS	98.2% ± 0.48%	99.6% ± 0.52%	99.3% ± 0.95%
60 Hz ASD	99.9% ± 0.32%	99.9% ± 0.32%	99.2% ± 1.32%
50 Hz ASD	67.4% ± 3.6%	91.2% ± 4.83%	86.9% ± 3%
40 Hz ASD	99.9% ± 0.01%	99.9% ± 0.01%	97.4% ± 3.41%
30 Hz ASD	99.4% ± 0.52%	99.9% ± 0.32%	80.2% ± 3.71%
20 Hz ASD	99.8% ± 0.42%	99.6% ± 0.52%	99.4% ± 1.07%
10 Hz ASD	94% ± 1.76%	96.5% ± 1.18%	99.7% ± 0.67%

Global Accuracy = 95.67, % Standard Deviation=1.38%

TABLE 11. Theoretical computational complexity of the methodology utilized.

	+/-	×	÷	√	AND	X-OR
MODWT	1098nm - 30	1098nm				
Mag	10nm	35nm				
FFT 2D	$MN \log_2(MN/2)$	$MN \log_2(MN)/2$				
Filter		5nm				
Binarization			5nm			
Laplacian						
Mask	8nm	9nm			8nm	9nm
Classification					10	

$n = 320, N = 512, m = 100, M = 128$  ( $\sim 10^8$  Basic operations)

TABLE 12. Comparison between fault Detection Methods.

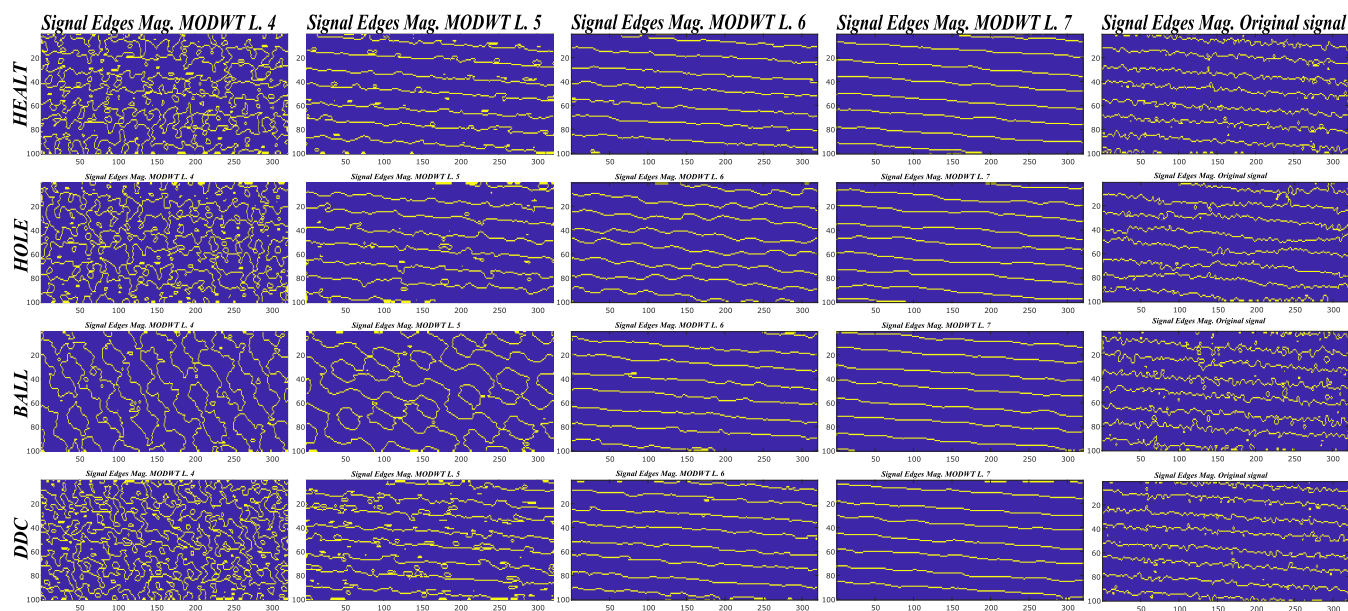
No	Ref	Methodology	No. operations
1	[42]	Kolmogorov Smirnov test	$\sim 10^4$
2	[42]	Kuiper test	$\sim 10^4$
3	[42]	Perason Chi-squared test	$\sim 10^4$
4	[43]	Sub-Nyquist Strategy With Reduced Data Length	$\sim 10^9$
5	[*]	Proposed	$\sim 10^8$
6	[44]	Estimation of Signal Parameters via Rotational Invariance Techniques	$\sim 10^{11}$
7	[23]	MODWT and a Lightweight 1D CNN	$\gg 10^{12}$

Table 8 shows the values of accuracy reached for tests performed with mechanical load, and here it is possible to notice that at 50 Hz specifically, the accuracy decreases when the IM is fed from an ASD, the accuracy at 30Hz decreases slightly, and for the rest of the cases it is presented in a value that exceeds 94 % (except for the BALL damage at 10 Hz). Thus, the MCSA methodology achieves an overall value of 92.43 % with the mechanical load.

Table 10 shows the values of accuracy achieved for MSCSA tests performed with a load. It can be seen that, especially at 60 Hz, the accuracy increases when the IM is fed from an ASD, unlike MCSA, in the case of 50 Hz, the accuracy decreases only for the case of HOLE damage, the accuracy does not decay at 30 Hz as with MCSA, the MSCSA methodology reaches overall values of 95.67 %. If the 50 Hz tests that presented problems were discarded, the accuracy for would be 97.74%.

## VI. CONCLUSION

The experimental results confirm the success of the proposed methodology implemented; they can be competitive compared with the state of the art results. In this work, current signals are used as input to the algorithms. As a result, MSCSA shows better accuracy results than MCSA.



**FIGURE 15.** Comparison between various types of patterns generated by MCSA for each type of damage using signals from a loaded IM fed by 60Hz ASD.

Furthermore, combining both methodologies according to the loading condition is recommended to ensure satisfactory accuracy results under general operating conditions. Furthermore, the ability to discern between different types of bearing damage shows the potential of the test to diagnose different types of damage according to their distribution, e.g., bearing damage, bar damage, short-circuit damage, among others. Furthermore, using simple statistical techniques by pattern counting shows the advantages of the presented methodology in BFD. Finally, the proposed algorithm has the flexible ability to work together with other BFD methodologies, such as using artificial neural networks to identify patterns in the two-dimensional arrays, facilitating the possibility of achieving accuracy improvements in future work.

#### APPENDIX A COMPUTATIONAL COMPLEXITY

Table 11 shows the computational cost of this methodology, which is high compared to others as a consequence of the wavelet transforms of 5 seconds of signal. In addition it is required to obtain the magnitude from the three phases of current to five sets of signals that come from the original signal and the four levels of wavelet transform.

Also, quite a lot of resources are consumed in the processing of the two-dimensional arrays through the FFT 2D, filtering, binarization and the Laplacian, once the masks are analyzed very simple binary operations of type X-OR and AND that manipulate the counter are performed, then the detector only uses comparison operations to classify based on the calibration parameters.

Table 12 shows the comparison between different methods according to their computational complexity. As can be seen, the computational cost is not low but neither is it as excessive

as the computational cost used by Deep Learning methods in [23]. In [43] there is also an analysis of computational costs prior to 2017 and it is worth noting the work published in [1] manages to reduce the computational cost by an order of magnitude with respect to the work published in [43].

#### APPENDIX B LINK BETWEEN THE FAULT TYPE AND THE STUDIED EDGE PATTERNS

Figure 7 is a 3D representation of two of the texture signals shown in figure 6, these when processed by the Gaussian filter change to a smoother texture shown in figure 8 and 9. Figure 10 is a two dimensional array with binary data: 0 (blue) and 1 (Yellow), these serve to detect 1 pixel wide edges presented in Fig 11 which is here where it is relevant to observe the various bearing conditions.

Fig. 15 shows the edge arrays obtained for each particular damage condition for a loaded IM, it can be clearly seen that the BALL and DDC are most easily distinguished by their patterns at the L4 and L5 wavelet levels, while the L6 level helps to distinguish the HOLE damage.

However, this is visible to the naked eye in the patterns, but the use of a mask to scan and quantify the patterns and compare them with a probability distribution uses each of the levels L4 to L6 as well as the original signal to determine the condition of the bearing or the type of damage that is present.

#### REFERENCES

- [1] V. Avina-Corral, J. Rangel-Magdaleno, C. Morales-Perez, and J. Hernandez, "Bearing fault detection in adjustable speed drive-powered induction machine by using motor current signature analysis and goodness-of-fit tests," *IEEE Trans. Ind. Informat.*, vol. 17, no. 12, pp. 8265–8274, Dec. 2021.

- [2] M. C. Pagaimo, J. F. P. Fernandes, M. Pérez-Sánchez, P. A. López-Jiménez, H. M. Ramos, and P. J. Costa Branco, "Transient study of series-connected pumps working as turbines in off-grid systems," *Energy Convers. Manage.*, vol. 245, Oct. 2021, Art. no. 114586.
- [3] A. Fourati, A. Bourdon, N. Feki, D. Rémond, F. Chaari, and M. Haddar, "Angular-based modeling of induction motors for monitoring," *J. Sound Vib.*, vol. 395, pp. 371–392, May 2017.
- [4] P. Balakrishna and U. Khan, "An autonomous electrical signature analysis-based method for faults monitoring in industrial motors," *IEEE Trans. Instrum. Meas.*, vol. 70, pp. 1–8, 2021.
- [5] R. R. Singh, R. Selvaraj, H. Mohan, and T. R. Chelliah, "Dynamic performance of doubly fed hydroelectric machines under voltage unbalance—A relative electrothermomechanical analysis," *IEEE Trans. Ind. Appl.*, vol. 54, no. 5, pp. 4156–4166, Sep./Oct. 2018.
- [6] J. L. Gonzalez-Cordoba, R. A. Osornio-Rios, D. Granados-Lieberman, R. D. J. Romero-Troncoso, and M. Valtierra-Rodriguez, "Correlation model between voltage unbalance and mechanical overload based on thermal effect at the induction motor stator," *IEEE Trans. Energy Convers.*, vol. 32, no. 4, pp. 1602–1610, Dec. 2017.
- [7] P. Gnaciński, D. Hallmann, P. Klimczak, A. Muc, and M. Pepliński, "Effects of voltage interharmonics on cage induction motors," *Energies*, vol. 14, no. 5, p. 1218, Feb. 2021.
- [8] Q. Lei, J. Yu, and Q.-G. Wang, "Discrete-time command filtered adaptive fuzzy fault-tolerant control for induction motors with unknown load disturbances," *J. Franklin Inst.*, vol. 358, no. 5, pp. 2765–2779, Mar. 2021.
- [9] T. Yang, H. Pen, Z. Wang, and C. S. Chang, "Feature knowledge based fault detection of induction motors through the analysis of stator current data," *IEEE Trans. Instrum. Meas.*, vol. 65, no. 3, pp. 549–558, Mar. 2016.
- [10] J. de Jesus Rangel-Magdaleno, H. Peregrina-Barreto, J. M. Ramirez-Cortes, P. Gomez-Gil, and R. Morales-Caporal, "FPGA-based broken bars detection on induction motors under different load using motor current signature analysis and mathematical morphology," *IEEE Trans. Instrum. Meas.*, vol. 63, no. 5, pp. 1032–1040, May 2014.
- [11] B. Patnaik, M. Mishra, R. C. Bansal, and R. K. Jena, "MODWT-XGBoost based smart energy solution for fault detection and classification in a smart microgrid," *Appl. Energy*, vol. 285, Mar. 2021, Art. no. 116457.
- [12] J. E. Garcia-Bracamonte, J. M. Ramirez-Cortes, J. de Jesus Rangel-Magdaleno, P. Gomez-Gil, H. Peregrina-Barreto, and V. Alarcon-Aquino, "An approach on MCSA-based fault detection using independent component analysis and neural networks," *IEEE Trans. Instrum. Meas.*, vol. 68, no. 5, pp. 1353–1361, May 2019.
- [13] B. Li, P. Zhang, D. Liu, S. Mi, G. Ren, and H. Tian, "Feature extraction for rolling element bearing fault diagnosis utilizing generalized S transform and two-dimensional non-negative matrix factorization," *J. Sound Vib.*, vol. 330, no. 10, pp. 2388–2399, 2011.
- [14] M. Singh and A. G. Shaik, "Faulty bearing detection, classification and location in a three-phase induction motor based on stockwell transform and support vector machine," *Measurement*, vol. 131, pp. 524–533, Jan. 2019.
- [15] A. Rai and S. H. Upadhyay, "A review on signal processing techniques utilized in the fault diagnosis of rolling element bearings," *Tribol. Int.*, vol. 96, pp. 289–306, Apr. 2016.
- [16] A. K. Verma, S. Nagpal, A. Desai, and R. Sudha, "An efficient neural-network model for real-time fault detection in industrial machine," *Neural Comput. Appl.*, vol. 33, no. 4, pp. 1297–1310, Feb. 2021.
- [17] S. Das, P. Purkait, D. Dey, and S. Chakravorti, "Monitoring of interturn insulation failure in induction motor using advanced signal and data processing tools," *IEEE Trans. Dielectr. Electr. Insul.*, vol. 18, no. 5, pp. 1599–1608, Oct. 2011.
- [18] M. Malekpour, B. T. Phung, and E. Ambikairajah, "Online technique for insulation assessment of induction motor stator windings under different load conditions," *IEEE Trans. Dielectr. Electr. Insul.*, vol. 24, no. 1, pp. 349–358, Feb. 2017.
- [19] M. Hernandez-Vargas, E. Cabal-Yepez, and A. Garcia-Perez, "Real-time SVD-based detection of multiple combined faults in induction motors," *Comput. Electr. Eng.*, vol. 40, no. 7, pp. 2193–2203, Oct. 2014.
- [20] A. G. Garcia-Ramirez, R. A. Osornio-Rios, D. Granados-Lieberman, A. Garcia-Perez, and R. J. Romero-Troncoso, "Smart sensor for online detection of multiple-combined faults in VSD-fed induction motors," *Sensors*, vol. 12, no. 9, pp. 11989–12005, 2012.
- [21] A. Garcia-Perez, R. de Jesus Romero-Troncoso, E. Cabal-Yepez, and R. A. Osornio-Rios, "The application of high-resolution spectral analysis for identifying multiple combined faults in induction motors," *IEEE Trans. Ind. Electron.*, vol. 58, no. 5, pp. 2002–2010, May 2011.
- [22] R. J. Romero-Troncoso, R. Saucedo-Gallaga, E. Cabal-Yepez, A. Garcia-Perez, R. A. Osornio-Rios, R. Alvarez-Salas, H. Miranda-Vidales, and N. Huber, "FPGA-based online detection of multiple combined faults in induction motors through information entropy and fuzzy inference," *IEEE Trans. Ind. Electron.*, vol. 58, no. 11, pp. 5263–5270, Nov. 2011.
- [23] M. Jimenez-Guarneros, C. Morales-Perez, and J. Rangel-Magdaleno, "Diagnostic of combined mechanical and electrical faults in ASD-powered induction motor using MODWT and a lightweight 1D CNN," *IEEE Trans. Ind. Informat.*, early access, Oct. 19, 2021, doi: 10.1109/TII.2021.3120975.
- [24] Z. Liu, L. Zhang, and J. Carrasco, "Vibration analysis for large-scale wind turbine blade bearing fault detection with an empirical wavelet thresholding method," *Renew. Energy*, vol. 146, pp. 99–110, Feb. 2020.
- [25] A. Djebala, M. K. Babouri, and N. Ouelaa, "Rolling bearing fault detection using a hybrid method based on empirical mode decomposition and optimized wavelet multi-resolution analysis," *Int. J. Adv. Manuf. Technol.*, vol. 79, nos. 9–12, pp. 2093–2105, 2015.
- [26] Z. Wang, Q. Zhang, J. Xiong, M. Xiao, G. Sun, and J. He, "Fault diagnosis of a rolling bearing using wavelet packet denoising and random forests," *IEEE Sensors J.*, vol. 17, no. 17, pp. 5581–5588, Sep. 2017.
- [27] M. E. Iglesias Martínez, J. A. Antonino-Daviu, P. F. de Córdoba, and J. A. Conejero, "Higher-order spectral analysis of stray flux signals for faults detection in induction motors," *Appl. Math. Nonlinear Sci.*, vol. 5, no. 2, pp. 1–14, Jul. 2020.
- [28] L. Saidi, J. Ben Ali, M. Benbouzid, and E. Bechhoefer, "The use of SESK as a trend parameter for localized bearing fault diagnosis in induction machines," *ISA Trans.*, vol. 63, pp. 436–447, Jul. 2016.
- [29] Q. Ni, J. C. Ji, K. Feng, and B. Halkon, "A fault information-guided variational mode decomposition (FIVMD) method for rolling element bearings diagnosis," *Mech. Syst. Signal Process.*, vol. 164, Feb. 2022, Art. no. 108216.
- [30] P. Ewert, T. Orłowska-Kowalska, and K. Jankowska, "Effectiveness analysis of PMSM motor rolling bearing fault detectors based on vibration analysis and shallow neural networks," *Energies*, vol. 14, no. 3, p. 712, Jan. 2021.
- [31] A. Youcef Khodja, N. Guersi, M. N. Saadi, and N. Boutasseta, "Rolling element bearing fault diagnosis for rotating machinery using vibration spectrum imaging and convolutional neural networks," *Int. J. Adv. Manuf. Technol.*, vol. 106, nos. 5–6, pp. 1737–1751, Jan. 2020.
- [32] I. Attoui, B. Oudjani, N. Boutasseta, N. Fergani, M.-S. Bouakkaz, and A. Bouraiou, "Novel predictive features using a wrapper model for rolling bearing fault diagnosis based on vibration signal analysis," *Int. J. Adv. Manuf. Technol.*, vol. 106, nos. 7–8, pp. 3409–3435, Jan. 2020.
- [33] K. Saini and S. S. Dhama, "MODWT and VMD based intelligent gearbox early stage fault detection approach," *J. Failure Anal. Prevention*, vol. 21, pp. 1821–1837, Sep. 2021.
- [34] Y. Cao, M. Jia, P. Ding, and Y. Ding, "Transfer learning for remaining useful life prediction of multi-conditions bearings based on bidirectional-GRU network," *Measurement*, vol. 178, Jun. 2021, Art. no. 109287.
- [35] F. Gougam, C. Rahmoune, D. Benazzouz, A. Afia, and M. Zair, "Bearing faults classification under various operation modes using time domain features, singular value decomposition, and fuzzy logic system," *Adv. Mech. Eng.*, vol. 12, no. 10, 2020, p. 1687814020967874.
- [36] E. Elbouchikhi, V. Choqueuse, and M. Benbouzid, "Induction machine bearing faults detection based on a multi-dimensional MUSIC algorithm and maximum likelihood estimation," *ISA Trans.*, vol. 63, pp. 413–424, Jul. 2016.
- [37] C. Morales-Perez, J. Grande-Barreto, J. Rangel-Magdaleno, and H. Peregrina-Barreto, "Bearing fault detection in induction motors using MCSA and statistical analysis," in *Proc. IEEE Int. Instrum. Meas. Technol. Conf. (I2MTC)*, May 2018, pp. 1–5.
- [38] W. Deng, S. Zhang, H. Zhao, and X. Yang, "A novel fault diagnosis method based on integrating empirical wavelet transform and fuzzy entropy for motor bearing," *IEEE Access*, vol. 6, pp. 35042–35056, 2018.
- [39] L. Bo, G. Xu, X. Liu, and J. Lin, "Bearing fault diagnosis based on subband time-frequency texture tensor," *IEEE Access*, vol. 7, pp. 37611–37619, 2019.
- [40] Q. Jiang, F. Chang, and B. Sheng, "Bearing fault classification based on convolutional neural network in noise environment," *IEEE Access*, vol. 7, pp. 69795–69807, 2019.
- [41] W. Fontes Godoy, D. Morinigo-Sotelo, O. Duque-Perez, I. Nunes da Silva, A. Goedtel, and R. H. C. Palácios, "Estimation of bearing fault severity in line-connected and inverter-fed three-phase induction motors," *Energies*, vol. 13, no. 13, p. 3481, Jul. 2020.

- [42] L. Yuan, D. Lian, X. Kang, Y. Chen, and K. Zhai, "Rolling bearing fault diagnosis based on convolutional neural network and support vector machine," *IEEE Access*, vol. 8, pp. 137395–137406, 2020.
- [43] A. Naha, A. K. Samanta, A. Routray, and A. K. Deb, "Low complexity motor current signature analysis using sub-nyquist strategy with reduced data length," *IEEE Trans. Instrum. Meas.*, vol. 66, no. 12, pp. 3249–3259, Dec. 2017.
- [44] Y. Trachi, E. Elbouchikhi, V. Choqueuse, and M. E. H. Benbouzid, "Induction machines fault detection based on subspace spectral estimation," *IEEE Trans. Ind. Electron.*, vol. 63, no. 9, pp. 5641–5651, Sep. 2016.



**VICTOR AVIÑA-CORRAL** (Graduate Student Member, IEEE) was born in Mexico City, Mexico. He received the B.E. degree in electronics engineering (specialty in digital systems) from the Instituto Tecnológico de Durango, Durango, Mexico in 2008, and the M.Sc. degree in electronics from the Instituto Nacional de Astrofísica, Óptica y Electrónica, Puebla, Mexico, in 2019, where he is currently pursuing the Ph.D. degree.

His research interests include FPGAs, DSP, instrumentation, control and automation, and power electronics.



**JOSE DE JESUS RANGEL-MAGDALENO** (Senior Member, IEEE) received the B.E. degree in electronics engineering and the M.E. degree in electrical engineering on hardware signal processing from the Universidad de Guanajuato, Mexico, in 2006 and 2008, respectively, and the Ph.D. degree from the Universidad Autónoma de Queretaro, Mexico, in 2011.

He is currently a Tenured Researcher at the Electronics Department, INAOE, Mexico. He has authored one book, and more than 100 works published in book chapters, journals, and conferences. His research interests include FPGAs, signal and image processing, and instrumentation.

Dr. Rangel-Magdaleno is a member of the Mexican National Research System (SNI), Level 2. He received the 2018 IEEE I&MS Outstanding Young Engineer Award.



**HAYDE PEREGRINA-BARRETO** (Senior Member, IEEE) received the bachelor's degree in computer science from the Instituto Tecnológico de Cuautla, in 2006, the master's degree in engineering from the Universidad de Guanajuato, in 2008, and the Ph.D. degree in engineering from the Universidad Autónoma de Queretaro, Mexico, in 2011. She made a postdoctoral research in medical imaging at the INAOE, Mexico, in 2014, where she is currently a Titular Researcher. She

has authored more than 40 works published in book chapters, journals, and conferences. Her research interests include image processing and medical imaging. She is a member of the Mexican National Research System (SNI).



**JUAN MANUEL RAMIREZ-CORTES** (Senior Member, IEEE) received the B.Sc. degree in electrical engineering from the National Polytechnic Institute, Mexico, the M.Sc. degree in electrical engineering from the National Institute of Astrophysics, Optics, and Electronics (INAOE), Mexico, and the Ph.D. degree in electrical engineering from Texas Tech University. Since 2007, he has been at the INAOE, where he has been the Electronics Department Chair and the Research

Director, where he is currently a Titular Researcher at the Electronics Department. His research interests include signal and image processing, biometry, neural networks, fuzzy logic, and digital systems. He was an Appointed Member of the Administrative Committee of the IEEE Instrumentation and Measurement Society. He is also serving as a Finance VP. He is a member of the Mexican National Research System (SNI), Level 2.

...